Acta Biomaterialia 8 (2012) 1469–1480

Contents lists available at SciVerse ScienceDirect

Acta Biomaterialia

journal homepage: www.elsevier.com/locate/actabiomat

Adhesion and cohesion in structures containing suspended microscopic polymeric films

W.L. Shan [a,b,c], J. Du [a,b], E.P. Hampp [a,b], H. Li [c], G. Papandreou [d], C.A. Maryanoff [c], W.O. Soboyejo [a,b,*]

[a] Princeton Institute for the Science and Technology of Materials, Princeton University, Princeton, NJ 08544, USA
[b] The Department of Mechanical and Aerospace Engineering, Princeton University, Princeton, NJ 08544, USA
[c] Cordis Corporation, Spring House, PA 19477, USA
[d] Cordis Corporation, Warren, NJ 07059, USA

ARTICLE INFO

Article history:
Received 20 August 2011
Received in revised form 6 December 2011
Accepted 12 December 2011
Available online 16 December 2011

Keywords:
Adhesive strength
Cohesive strength
Suspended microscopic polymeric films
Finite element modeling
Stents

ABSTRACT

This paper presents a novel technique for the characterization of adhesion and cohesion in suspended micro-scale polymeric films. The technique involves push-out testing with probes that are fabricated using focused ion beam techniques. The underlying stresses associated with different probe tip sizes were computed using a finite element model. The critical force for failure of the film substrate interface is used to evaluate adhesion, while the critical force for penetration of the film determines cohesion. When testing a standard material, polycarbonate, a shear strength of approximately 70 MPa was calculated using the Mohr–Coulomb theory. This value was shown to be in agreement with the results in the literature. The technique was also applied to the measurement of adhesion and cohesion in a model drug-eluting stent (the Nevo™ Sirolimus Eluting Coronary Stent) containing suspended microscopic polymeric films in metallic Co–Cr alloy reservoirs. The cohesive strength of the formulation was found to be comparable with that of plastics such as those produced by reaction injection molding and high-density polyethylene.

1. Introduction

In the rapidly expanding fields of medical devices and microelectronics thin polymeric films have enhanced the properties of the systems they coat [1]. For example, the results obtained from prior work suggest that in cases where formulations of drugs and polymers have been applied to stents the resulting drug-eluting stents result in reduced restenosis, the re-narrowing of treated arteries, over their metallic counterparts [1]. The adhesion of such films to their substrates has been the subject of several studies [2–9].

Nano-mechanical tests have been developed to gain an insight into the adhesion and the fundamental mechanical properties of thin films [2–6]. In these tests a stylus first comes into contact with a sample, which is then indented to shallow nano-scale depths. In the nanoindentation test a normal force is applied to the tip and its displacement is recorded [2]. A stress is induced in the film surrounding the indenter that can initiate and propagate interfacial cracks.

Single/multiple indents (as in ISO method 14577) have also been used to measure hardness, the Young's modulus, and interfacial fracture toughness of thin films, thick coatings and bulk materials [3–6]. The indentation interfacial toughness, a direct measure of adhesion, can be estimated by analyzing the indented area. For example, a nanoindentation method was used to evaluate the adhesion strength of poly(N-isopropylacrylamide) co-polymers on nitinol wires [5]. The interfacial fracture toughness G varied from 0.1 to 0.3 J m^{-2}, depending on the surface roughness of the film.

The nanoscratch test consists of application of vertical and lateral forces to the tip [3,4]. Using either constant or progressive forces the critical load that provokes coating detachment can be measured. This measurement is then used to evaluate scratch hardness and scratch adhesion of the thin films. For example, to evaluate the relative adhesion of the coatings of three commercial drug-eluting stents to their corresponding substrates the forces to induce delamination between the coating and the stent were measured by a nanoscratch method and were found to be comparable [6].

In previous works [7–9] we have used a combination of models and experiments to study the adhesion between soft films and hard substrates. Atomic force microscopy (AFM) [7] and interfacial fracture mechanics techniques [8,9] were used to measure the adhesion between different interfaces within and between the coated substrates. A combination of adhesion theory and interfacial fracture mechanics models was then used to obtain adhesion

* Corresponding author at: The Department of Mechanical and Aerospace Engineering, Princeton University, Princeton, NJ 08544, USA.
E-mail address: soboyejo@aol.com (W.O. Soboyejo).

1742-7061/$ - see front matter © 2011 Acta Materialia Inc. Published by Elsevier Ltd. All rights reserved.
doi:10.1016/j.actbio.2011.12.018

energy measurements for a wide range of interfaces between hard and soft materials with different chemistries [7].

An orthogonal interfacial fracture mechanics method [8,9] has also been used to corroborate the AFM measurements of adhesion. In this method layers of the film were independently applied to metallic disks. These disks were sandwiched to form Brazil nut sandwich specimens that mimic the chemistries of the films on the stents. These specimens were deformed continuously until interfacial failure was induced from notches that were oriented at different angles to induce mixed modes between pure mode I and pure mode II. Hence, using the Cypher® Sirolimus Eluting Coronary Stent as an example [9], the adhesion energy of every interface of the coating, consisting of a Parylene C primer layer and a drug-eluting layer of sirolimus, poly(*n*-butyl methacrylate) and poly(ethylene-co-vinyl acetate) on 316L stainless steel was quantified and verified.

Although the above methods provide ways of measuring the adhesion between thin films and conforming substrates, there are currently no methods for measuring the adhesion of a film that has limited contact with the substrate, i.e. a suspended film. For example, in the case of the Nevo™ Sirolimus Eluting Coronary Stent (NSES) the formulation is suspended within several hundred reservoirs (length 120 μm × width 80 μm × depth 100 μm) that are filled with a formulation of sirolimus and the degradable polymer *poly(lactic-co-glycolic acid)* (PLGA) (Fig. 1). A mixture of sirolimus and PLGA is dissolved in solvent. The formulation is introduced into the reservoirs by a nanojet spraying method. After solvent evaporation the film remains suspended in the reservoir. The stent is fabricated from an L605 (Co–Cr) alloy. Hence, unlike stents with conformal coatings, the NSES contains formulation inlays within the stent reservoirs. AFM and nanoscratch styli cannot normally measure adhesion to the steep walls or overhangs. There is, therefore, a need to develop a novel technique for the measurement of adhesion between the formulation and the L605 alloy substrates and/or cohesive failure within the formulation layer.

The objective of this paper is to present a new method to measure the adhesive and cohesive strengths of suspended polymeric films. Inspired by ASTM Standard Test Method D732 [10], the technique involves the use of a micron-scale probe in the application of loads to suspended polymeric films that are mounted within a customized micro-tester. After the measurement of critical loads on a standard reference material, polycarbonate, the shear strength of the standard material is then calculated and compared with prior measurements of the mechanical properties of thin films. When used to evaluate NSES probes with small cross-sectional areas, relative to the cross-sections of the suspended polymeric films, are shown to result in cohesive failure, while probes with larger cross-sectional areas result in adhesive failure between the formulation films and the Co–Cr substrate. The measured adhesive and cohesive strengths are compared with measurements obtained in control experiments.

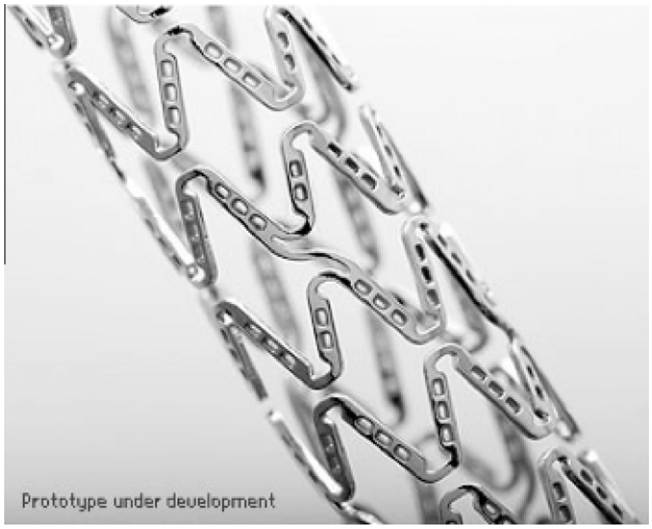

Fig. 1. Optical microscopy image of the NSES.

2. Experimental methods

2.1. Polymeric film adhesion and cohesion strengths testing

A schematic of the suspended film adhesion and cohesion strengths testing system is presented in Fig. 2. It consists of an actuator that is driven electronically by a wave generator to apply loads to the formulation film in the stent system (Fig. 1). The sample was clamped to a mechanical stage that was mounted on an anti-vibration table. A wave generator was used to generate the desired waveforms to input in a piezo-transducer (PZT) controller. The signals were amplified and used to drive the PZT. The loads from the PZT controller were applied in series to a tungsten probe (Fig. 2) (AutoProbe™ 300, Omniprobe, Dallas, TX) with a tip geometry that was micro-machined using an FEI Strata 235 dual beam focused ion beam (FIB) workstation. The loads were transduced through a 50 g load cell (Model 530, Coopers Instruments, Warrenton, VA) that was connected directly to a computer. In this way load data were acquired continuously throughout the measurements.

In an effort to immobilize the samples during testing these were clamped to a specially designed and machined fixture that was mounted on an *x*–*y* mechanical stage, as shown in Fig. 2. The clamping fixture system consisted of four layers. The bottom layer was a poly(methyl methacrylate) (PMMA) substrate, while the middle two layers were stainless steel sheets with identical grooved geometries. The top layer consisted of a thicker stainless steel sheet with a rectangular hole of the same size as the groove area of the middle two. The sample was sandwiched between the middle two layers. All four sheets were clamped with four cap screws and bolts along the length and width of the substrate.

To facilitate in situ imaging two digital Proscope HR™ (Bodelin Technologies, Lake Oswego, OR) microscopes were oriented perpendicularly to each other. The positioning of the probe (relative to the inlay) was achieved by aligning the *x*–*y* mechanical stage during in situ imaging. A photograph of the digital microscopes and the loading/mounting fixtures is presented in Fig. 2. These were used to obtain videos during push-out testing of the suspended polymeric films. The local curvatures of the films around the probe tip upon application of penetration forces were estimated from the video recordings.

The suspended film adhesion and cohesion strengths tests were conducted on NSES samples (Fig. 1) provided by Cordis Corporation. The specimens were first expanded to separate the stent from its delivery catheter. They were then cut, flattened, and inserted into the test fixture immediately after opening the package. The flattened specimens were then subjected to testing in air within 3 h of exposure to the laboratory environment. The laboratory air had a relative humidity of 38–55% and a temperature of 20–25 °C. The loading was carried out under displacement control at a constant rate of 40 μm s^{-1}.

NSES samples that were subjected to the adhesion/cohesion tests were analyzed in a Zeiss EVO scanning electron microscope (Carl Zeiss SMT Inc., Peabody, MA). Scanning electron microscopy (SEM) micrographs were obtained for both adhesive failure and cohesive failure, while energy dispersive spectroscopy (EDS)

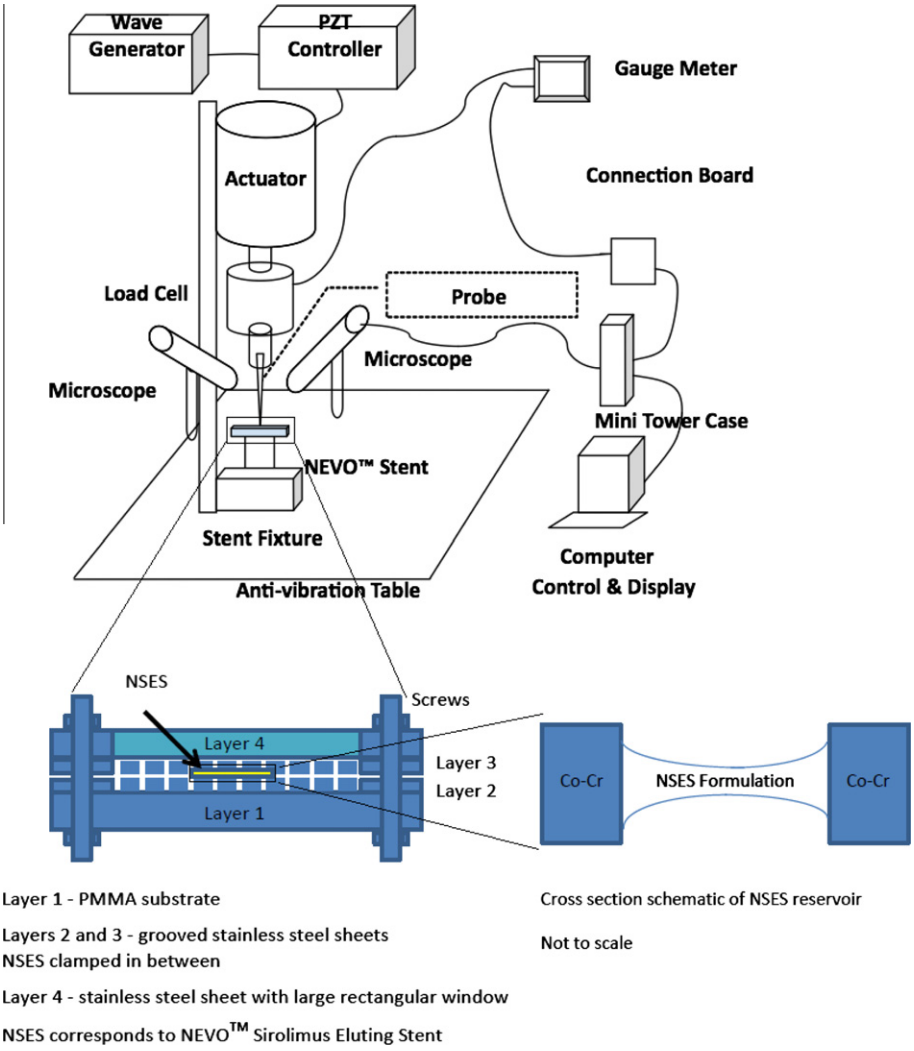

Fig. 2. Schematic of the suspended film adhesion and cohesion testing systems.

analysis was also carried out on specimens in which adhesive failure was observed. This was done to confirm that there was no residual formulation attached to the reservoir side walls.

2.2. Probe size design and fabrication

In the suspended film strength tests a tungsten probe was used to apply loads to thin suspended films surrounded by hard substrates. Finite element modeling (FEM) was used to design the proper probe tip sizes required for adhesive failure (between the substrate and the polymeric film) and cohesive failure (within the suspended polymeric film). This was achieved by using a finite element model to study the effects of probe tip size on the stress distributions in the polymeric/metallic composite structure. The Abaqus™ finite element software package (Abaqus is a trademark of Dassault Systemes Simulia Corp., Providence, RI) was used to compute the stress distributions associated with different probe tip sizes that induce cohesive and adhesive failure, respectively.

An axisymmetric model was used as a simplification of the three-dimensional geometry. In this model the probe was approximated as a cylinder, while the reservoir was approximated as a hollow cylinder that contains the polymer film. The thicknesses of the surrounding metal and the geometry of the suspended film were based on simplified geometries of NSES. The length of the probe tip was 80 μm.

The finite element model is presented in Fig. 3. It was assumed that all the materials exhibited isotropic elastic behavior, with mechanical properties that are summarized in Table 1. Considering the size and the geometry of the formulation inlay it is extremely challenging to use nanoindentation or microtesting techniques to measure the modulus of the formulation inlay, especially under conditions with well-controlled solvent contents. Potential variations can occur in the modulus of the formulation inlay as a function of the solvent content. Moreover, considering the unknown effects of mixing the drug and the PLGA polymer, the Young's modulus of the formulation was taken as that of PLGA. The modulus variations may cause some variations in the computed stress distributions.

The axisymmetric boundary condition was applied at the symmetry axis, as shown in Fig. 3. Also, the outside edge of the stent was fixed so as to undergo no displacement and rotation. Vertical displacement was applied to the top of the probe. The adhesive interactions allowed no relative displacement between the probe and the formulation inlay once the two surfaces made contact. Tangential behavior was used in the contact model, which assumed no slip between the probe and the surfaces of the formulation.

The size of the probe has important ramifications for the force measurements. Too small a probe can easily penetrate the formulation film, leading to cohesive failure, while a larger probe can

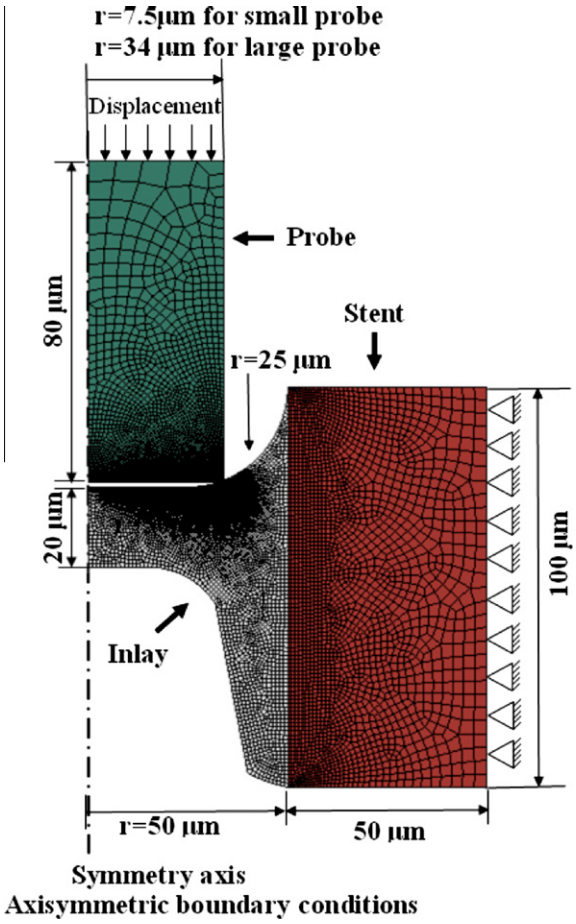

Fig. 3. Finite element model of the suspended film adhesion and cohesion tests.

Table 1
Mechanical properties used in FEM of the test method development.

Materials	Young's modulus	Poisson's ratio	Reference
Tungsten	410 GPa	0.28	[12]
Co–Cr	243 GPa	0.3	[13]
PLGA 75/25	629.3 MPa	0.3	[14]

dislocate the entire inlay and induce adhesive failure along the film/strut interface. Therefore, two simulations, one with a relatively small probe and one with a relatively large probe, were performed to demonstrate the effects of probe dimensions.

2.3. Performance of the test method

In order to produce reliable data from the test system the system was periodically calibrated. Calibration involved the application of loads using a set of standard weights from the National Institute of Standards and Technology (NIST) and measurement of the corresponding voltage outputs from the load cell for six different weights, each with six repetitions. This calibration result will be used later in the determination of adhesion and cohesion forces.

Measurements on a material with known properties were conducted and analyzed to verify the performance of the test method. A Sterlitech™ polycarbonate hydrophilic membrane filter (SPHMF) (Sterlitech Corp., Kent, WA) was used for the performance test as we were limited by the availability of commercial materials with

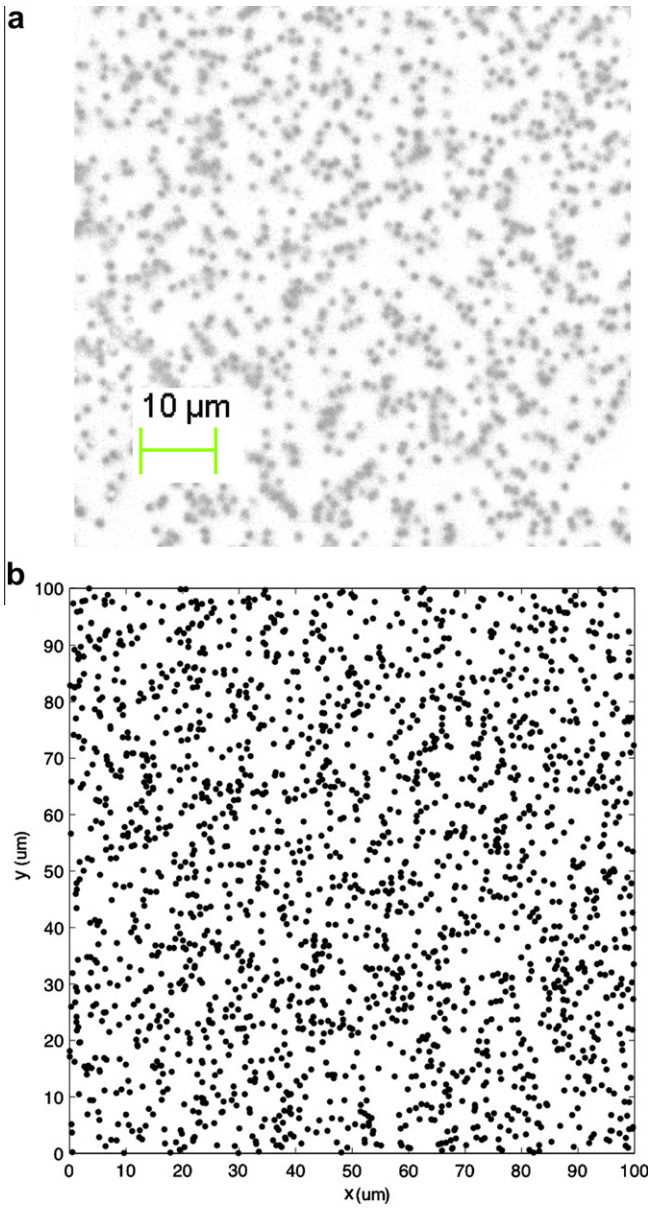

Fig. 4. (a) SEM micrograph of the SPHMF sample. (b) Monte Carlo simulation of the SPHMF sample.

a thickness of ~10 μm. This track etched membrane filter was made of Markolon® GP polycarbonate sheet by Bayer Material Science AG, with a thickness of 11 μm, and it contained isolated cylindrical holes (pores) with a radius r_0 of 0.5 μm. The pore density was $\alpha = 2 \times 10^7\ \mathrm{cm}^{-2}$ (Fig. 4a). The SPHMF was clamped in the mounting fixture (Fig. 2) and a total of 20 iterations of SPHMF penetration tests with probes with tip geometries of 10×20 μm and 45×90 μm were completed and analyzed.

An ANOVA gauge repeatability and reproducibility (Gauge R&R) test was also performed to assess the variability of the testing system, the method and the operators conducting the experiments. This test involved the use of two medium sized probes (cross-section 35×70 μm) to penetrate through the SPHMF sample. A total of 10 iterations of penetration tests were conducted by each of the two independent operators on three consecutive days.

Finally, a daily suitability check was designed, based on the results of the Gauge R&R test. In this test the same probes as used in the stent tests were used to penetrate a SPHMF sample clamped to the mounting fixture by one operator, with five iterations. The tests

on the NSES samples were only carried out when the average penetration force and sample standard deviation did not exceed the expected ranges.

3. Modeling

Although we recognize that interfacial and cohesive failure involve the initiation and growth of cracks, we will explore a simple strength approach for the characterization of cohesive and adhesive strengths in this section.

3.1. Modeling of the test method on SPHMF

When a rectangular or circular probe penetrates vertically downwards through an infinite membrane the measured penetration force F can be related to the critical shear stress of the membrane τ. This is given by:

$$\tau = F/A \tag{1a}$$

where $A = tC\delta$ is the sheared area, t is the thickness of the SPHMF samples, C is the circumference of the probe tip, and $\delta < 1$ is a correction factor since the SPHMF samples have randomly populated pores, which effectively reduce the sheared area in the penetration process. Thus:

$$\tau = F/tC\delta \tag{1b}$$

The value of δ for the SPHMF test using a rectangular or circular probe can be determined by solving a simplified two-dimensional problem, recognizing the fact that the thickness dimension of the SPHMF can be neglected in the problem herein.

To calculate δ for the SPHMF test using a rectangular probe a two-dimensional Monte Carlo simulation was carried out using the results for the plane geometry. First, it was assumed that fracture of the SPHMF sample occurred along the circumference of the probe tip. Then, without loss of generality, a square of edge length $L = 100$ μm was used as the SPHMF sample (Fig. 4b), while the circumference of the rectangular tip C can be approximated as a horizontal straight line of the same length C. Furthermore, the randomly distributed circular holes were approximated as circles with radius $r_0 = 0.5$ μm. The origins of the randomly populated circles were then added by assigning uniformly distributed points to the square. The number of the distributed circles was determined by multiplying the circle density α by the total area of the square L^2, i.e. $\alpha L^2 = 2000$ (Fig. 4b). For each realization the straight line segments that fall in the randomly distributed circles were calculated and summarized to obtain the accumulated length C_{al}. Multiple realizations were generated and the average accumulated length C_{aal} was thus obtained.

Using the estimated value of C_{aal} the correction factor δ for the circumferences was calculated from:

$$\delta = (C - C_{aal})/C \tag{2}$$

Similarly to the rectangular probe case, the correction factor δ for the SPHMF sample using a probe with a circular cross-section was also calculated using Monte Carlo simulations in the same manner as described above.

Unlike the ASTM D732 case, where the special fixting ensures no tension of the sheared material, during this SPHMF test a local curvature will develop as the probe goes further downward and the membrane extends accordingly. Therefore the shear strength, or the ultimate shear strength of the material τ_{uss}, was calculated according to the Mohr–Coulomb theory [11]. This gives:

$$\tau_{uss} = \tau - \sigma \tan(\theta) \tag{3}$$

where τ is the critical shear stress over the sheared area (obtained from the experimental measurements), σ is the normal stress on the sheared area (positive value for compression and negative value for tension), and θ is the angle of internal friction.

To obtain σ and θ a simplified axisymmetric free body diagram of the membrane immediately under the probe tip is shown in

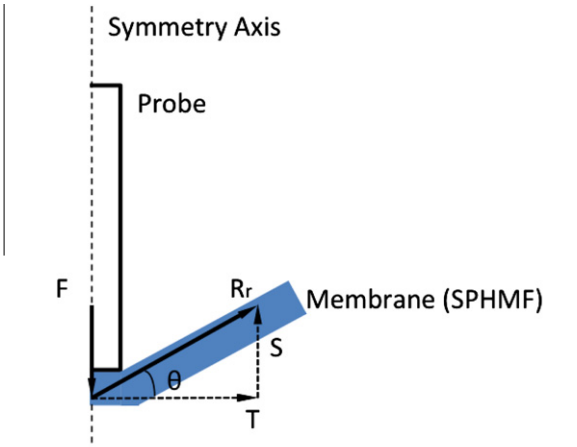

Fig. 5. Simplified axisymmetric free body diagram of the membrane section under the probe tip.

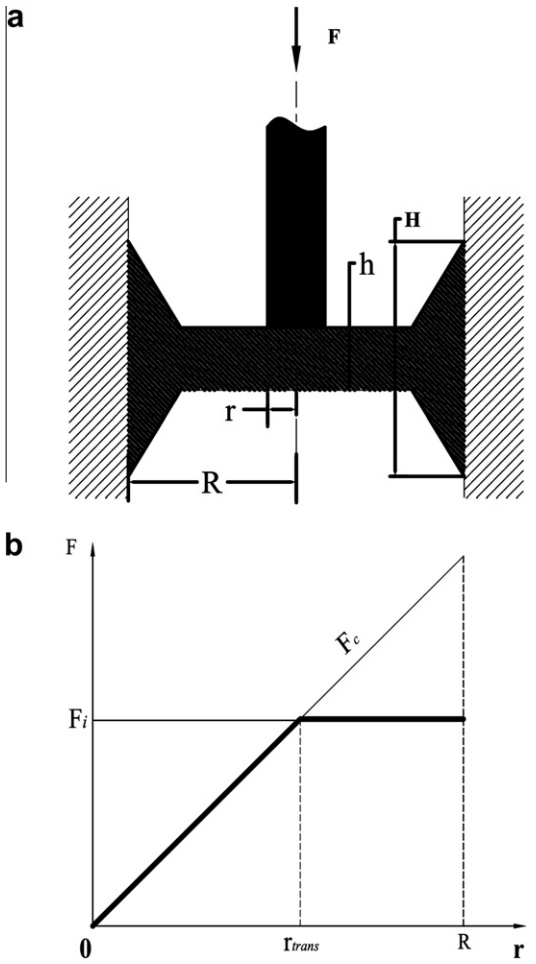

Fig. 6. (a) A simplification of the testing system for NSES. (b) Failure mode transitions in NSES testing.

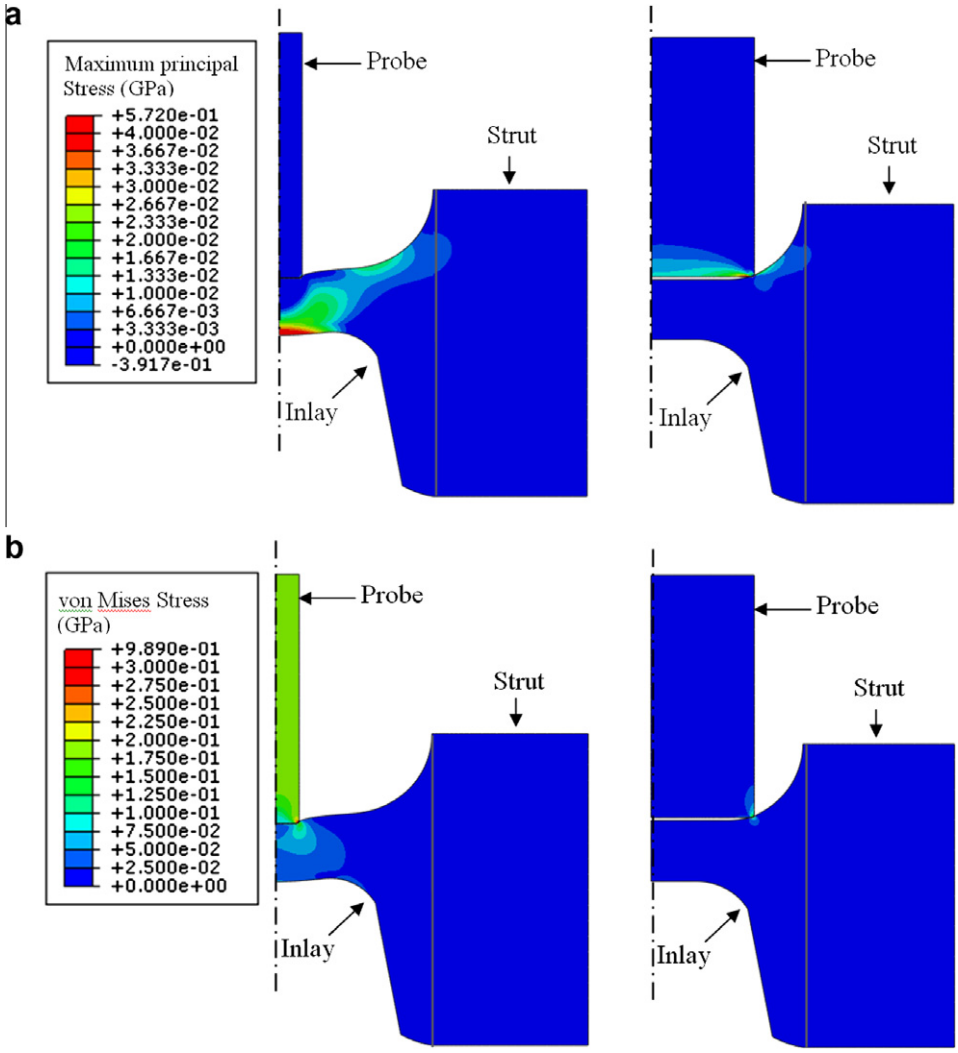

Fig. 7. (a) Maximum principal stress distributions in deformed NSES models for the same loads using the small and large probes. (b) Von Mises stress distributions in deformed NSES models for the same load using the small and large probes.

Fig. 5, where F is the applied probe force, which is then transferred to the circular membrane section with radius r, R_r is the reaction force from the surrounding membrane to the circular membrane section, which can be resolved into T and S, the horizontal and the vertical component forces exerted by the surrounding membrane, respectively (Fig. 5). The angle of internal friction is the angle between the local tangent of membrane curvature (direction of R_r) and T, which is the tension force on the sheared area. Thus, from force balance on s circular membrane section with radius r the following expressions are obtained:

$$S + F = 0 \tag{4a}$$

$$T\tan(\theta) = S \tag{4b}$$

Similarly to Eq. (1b), due to the presence of randomly distributed pores in the SPHMF samples, we have:

$$\sigma = T/(t2\pi r\delta) \tag{4c}$$

Hence, replacing $2\pi r$ with circumference C and combining Eqs. (1b), (3), (4a), and (4c) gives:

$$\tau_{uss} = 2F/(tC\delta) \tag{4d}$$

Thus an estimate of the shear strength of the polycarbonate material, based on the Mohr–Coulomb theory [11], is given by Eq. (4d). This can be obtained from the measured force F and geometrical parameters (δ, C and t).

3.2. Modeling of adhesion/cohesion in the NSES test

Consider the general case of a force applied to a circular probe that was used to push against a suspended film, as shown in Fig. 6a. In the case where interfacial stresses are sufficient to induce failure between the side walls and the polymeric film the interfacial shear strength τ_i is given by:

$$\tau_i = F_i/(2\pi RH) \tag{5}$$

where F_i is the force required to induce interfacial failure, R is the radius of the polymeric film, and H is the depth of the interface (Fig. 6a). Similarly, for smaller probe sizes cohesive failure may occur when a cohesive circumferential crack is induced around the probe tip and pushed through the film thickness. In such a scenario, a lower bound estimate of the cohesive strength is given by the condition in which the crack has propagated completely through the thickness. This gives:

$$\tau_c = F_c/(2\pi rh) \tag{6}$$

where F_c is the force required to induce cohesive failure, r is the probe tip radius, and h is the thickness of the film in the middle section. Since τ_i and τ_c may be considered measurements of "strength", then the transition from cohesive failure to adhesive failure may be determined from the critical condition at which the force required for interfacial failure F_i becomes equal to that required for cohesive failure F_c. From Eqs. (5) and (6) this critical condition, i.e. $F_i = F_c$, gives:

$$2\pi\tau_i RH = 2\pi\tau_c r_{trans} h \tag{7a}$$

or

$$r_{trans} = RH\tau_i/(\tau_c h) \tag{7b}$$

where r_{trans} denotes the probe size when the transition occurs. When $r < r_{trans}$ we have $F_c < F_i$ and the suspended film undergoes cohesive failure when the applied external force F reaches F_c first; when $r > r_{trans}$ we have $F_c > F_i$ and the suspended film undergoes adhesive failure when the applied external force F reaches F_i first. Hence, a transition should occur from cohesive failure at small probe tip radii to interfacial failure at larger probe tip radii, with a critical probe size r_{trans} given by Eq. (7b), as shown schematically in Fig. 6b. Thus the cohesive strength can be determined from the cohesive failure induced by a small probe, while adhesive strength can be determined from adhesive failure induced by a large enough probe.

4. Results and discussion

4.1. Finite element modeling and probe design/fabrication

To determine the appropriate probe size FEM was performed. This was used to simulate the interaction between several probes and a suspended film. A displacement was applied to the top of the pins until the reaction force reached the same value. The maximum principal stresses distributions and Von Mises stresses distributions obtained from the finite element models for the two probe sizes are shown in Fig. 7a and b. Note that since the mechanical properties of the formulation were estimated from those of its main component PLGA [14], it was assumed that the Von Mises equivalent stress is associated with plasticity definition of the formulation film. The magnitudes of the maximum stresses would increase slightly with further decreases in mesh size, however, the trends in the stress distribution should remain the same. Fig. 7a shows color contours of the maximum principal stress distributions that characterize the direction-independent values of stress that can induce failure, while Fig. 7b shows color contours of the Von Mises stresses that can affect the potential onset of plasticity. In both sets of stresses the stresses are highest underneath the probe. However, the stresses near the edges, where the formulation inlay is in contact with the Co–Cr stent material, are also high. As the probe displacement increases the stresses at the formulation inlay and Co–Cr strut interface increase, until they are sufficient to promote interfacial failure and inlay push-out.

Based on the FEM results two failure modes are possible for NSES stents. One is that at the interface between the formulation inlay and the Co–Cr alloy strut the stress is high enough for the interface to fail first. A crack will nucleate and grow along the interface until the whole structure fails, which results in adhesive failure. The other mode involves the nucleation and growth of a crack from regions of high stress distribution in the formulation underneath the probe. This will result in cohesive failure. The interplay between these two possible modes of failure will determine how the structure fails.

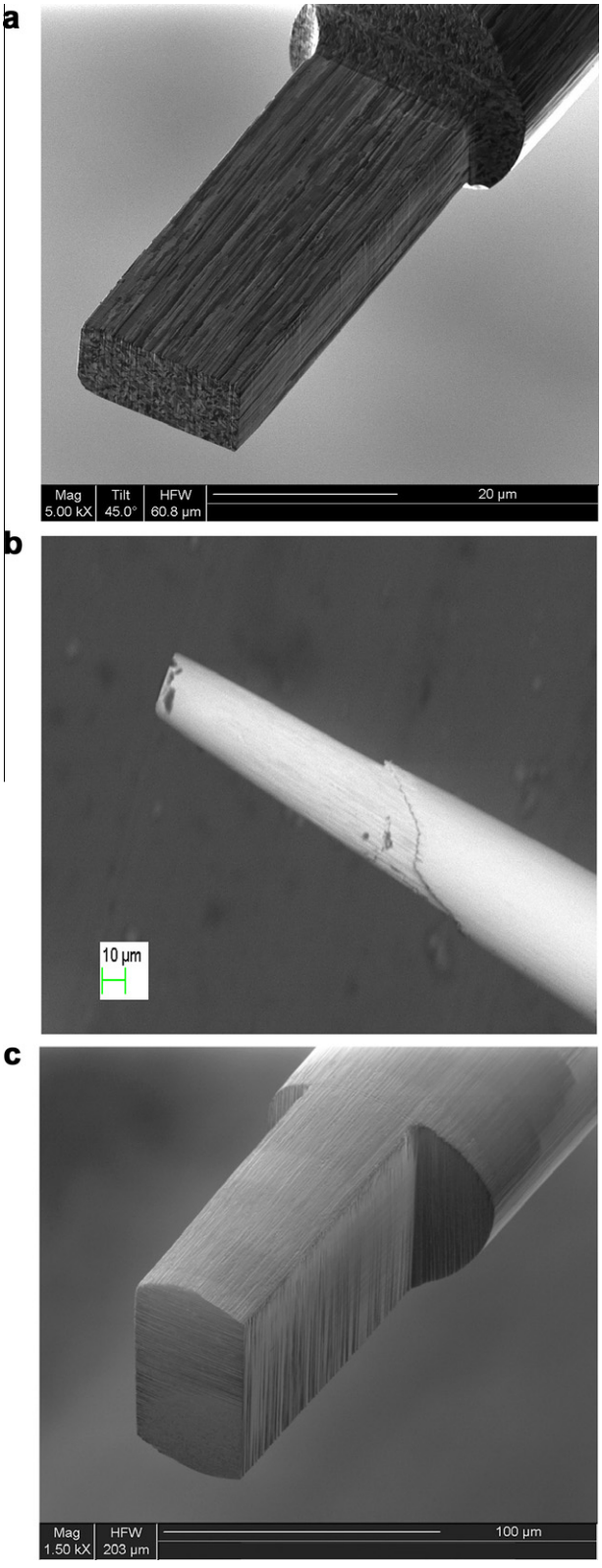

Fig. 8. (a) Cross-section with the small tungsten probe, 10 × 20 µm. (b) Circular cross-section with the small tungsten probe with a diameter of 20 µm. (c) Cross-section with the large tungsten probe, 45 × 90 µm.

For the same load the stress distributions beneath the probe decreased greatly with increasing probe tip size, while the stresses along the interface between the inlay and the strut remained at the same level. This suggests that the larger probe tip is more likely

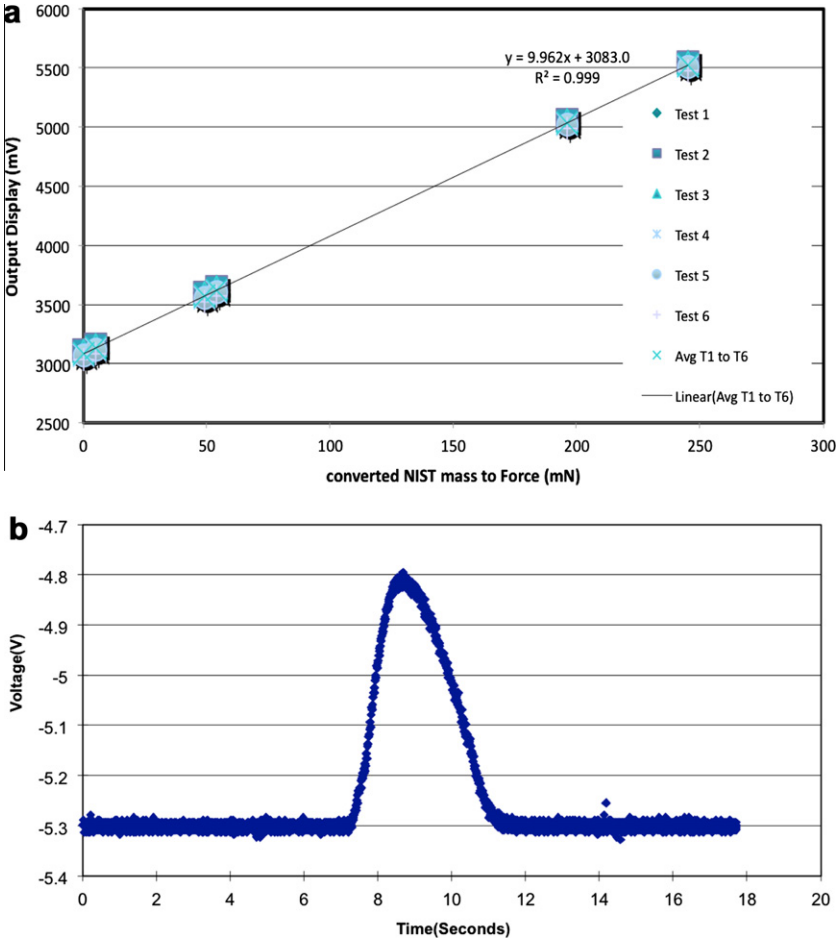

Fig. 9. (a) Calibration of the adhesion and cohesion characterization system using the NIST standard mass. (b) Typical voltage–time output during the adhesion and cohesion test.

to promote adhesive failure than cohesive failure. These computational results confirmed the theoretical prediction of a transition from cohesive failure to adhesive failure as the probe size increases.

The probe size determination was guided by the FEM presented above. Based on the results three probes with different tip sizes and shapes were fabricated using FIB techniques (Fig. 8a–c). The rectangular cross-sections (10×20 μm) and (45×90 μm) were selected as having similar aspect ratios to the rectangular reservoirs and corresponding to the probe sizes used in the FEM, while a circular cross-section with a diameter of 20 μm, roughly the same circumference as the small rectangular probe (~60 μm), was selected as a contrast to the geometrical effects on the measurements. They were used to induce both cohesive and adhesive failure in the stent tests.

4.2. Experiments on standard materials

The relationship between load and voltage was obtained for the micro-test system using a series of NIST standard weights. This is presented in Fig. 9a, while a typical plot of voltage versus time is shown in Fig. 9b. This correlation exhibited a linear relationship between voltage and force ($r^2 = 0.999$). Hence a combination of the calibration curve and the voltage outputs was used to measure the forces during the push-out tests.

The average failure loads (from 20 push-out tests) and the sample standard deviations (SSD) for the SPHMF penetration test were 21.3 ± 5.2 mN for probe tip dimensions of 10×20 μm, 22.9 ± 5.5 mN for the circular probe tip with a diameter of 20 μm, and 91.7 ± 12.8 mN for probe tip dimensions of 45×90 μm (Table 2). The Gauge R&R test also revealed that the effects of various factors on the measured forces, including the operators, testing time, probe number and SPHMF sample number, could not be determined. Therefore, it was appropriate to reduce the number of tests to five, without an impact on the results. This helped establish the sampling plan for testing of the NSES samples.

Due to the presence of the pores in SPHMF a correction factor was needed to obtain the polycarbonate shear strength from the measured forces. This required the computation of a correction factor using a Monte Carlo simulation in Matlab. A scanning electron micrograph of the porous structure of the membrane is presented in Fig. 4a. Fig. 10a and b shows snapshots of the random realization of the circle-populated squares for the rectangular cross-section case, while Fig. 10c and d shows snapshots of the random realization of the circle-populated squares for the circular cross-section case. The correction factor δ was 0.84, for both the rectangular and circular cross-section cases when the circle radius $r_0 = 0.5$ μm, the circle density $\alpha = 2 \times 10^7$ cm^{-2} and 10,000 realizations were taken to determine the average. The SEM images of the penetrated SPHMF samples further verified the assumption made earlier in the derivation of δ that the SPHMF samples will fail along the circumference of the probes (Fig. 11–c).

Note that in these models we essentially ignore the case in which two circles may intersect each other. If the circle density is low, then this can be ignored without much effect on the final results. Also, the two open ends of the straight line compensate for the effects of the four corners in the rectangular cross-section

Table 2
Shear strength of SPHMF polycarbonate determined in the performance test and taken from the literature.

Probe size	SPHMF Critical force (mN)	SPHMF polycarbonate Shear strength (MPa)	Markolon® GP Shear strength (MPa)
10 × 20 μm	21.3 ± 5.2	76.8 ± 18.7	68.9
45 × 90 μm	91.7 ± 12.8	73.5 ± 10.3	
20 μm diameter	22.9 ± 5.5	78.9 ± 18.9	

case. Furthermore, $\delta = 0.84$ corresponds to a convergent value when the penetration tests were performed a sufficient number of times. To illustrate the notion, since in our experiments 20 repetitions were completed for the SPHMF penetration test, similarly 20 realizations by Matlab were completed once for the rectangular cross-section case, and a correction factor of 0.84 ± 0.05 (mean ± SSD) was obtained. Thus in the calculation of polycarbonate membrane shear strength a constant value of 0.84 was used as a correction factor.

Using video monitoring curvature was observed for all the penetration tests that were performed on the SPHMF samples. An angle of 30° was also estimated for the internal friction angle θ. Therefore, to obtain the shear strength of the polycarbonate material that was tested the Mohr–Coulomb theory was applied. Using the corrections described above the shear strengths of the SPHMF polycarbonate material were calculated from measured forces, and are presented in Table 2, where they are compared with the shear strength for Markolon® GP Polycarbonate (http://www.plasticsintl.com/datasheets/Polycarbonate.pdf, 2011). The results obtained for all of the three probes are in good agreement with previously published results. This suggests that the geometrical effects of the probe tip shape are negligible and that the testing method yields results that can be correlated with those obtained from tests that were guided by ASTM D732-10 [10].

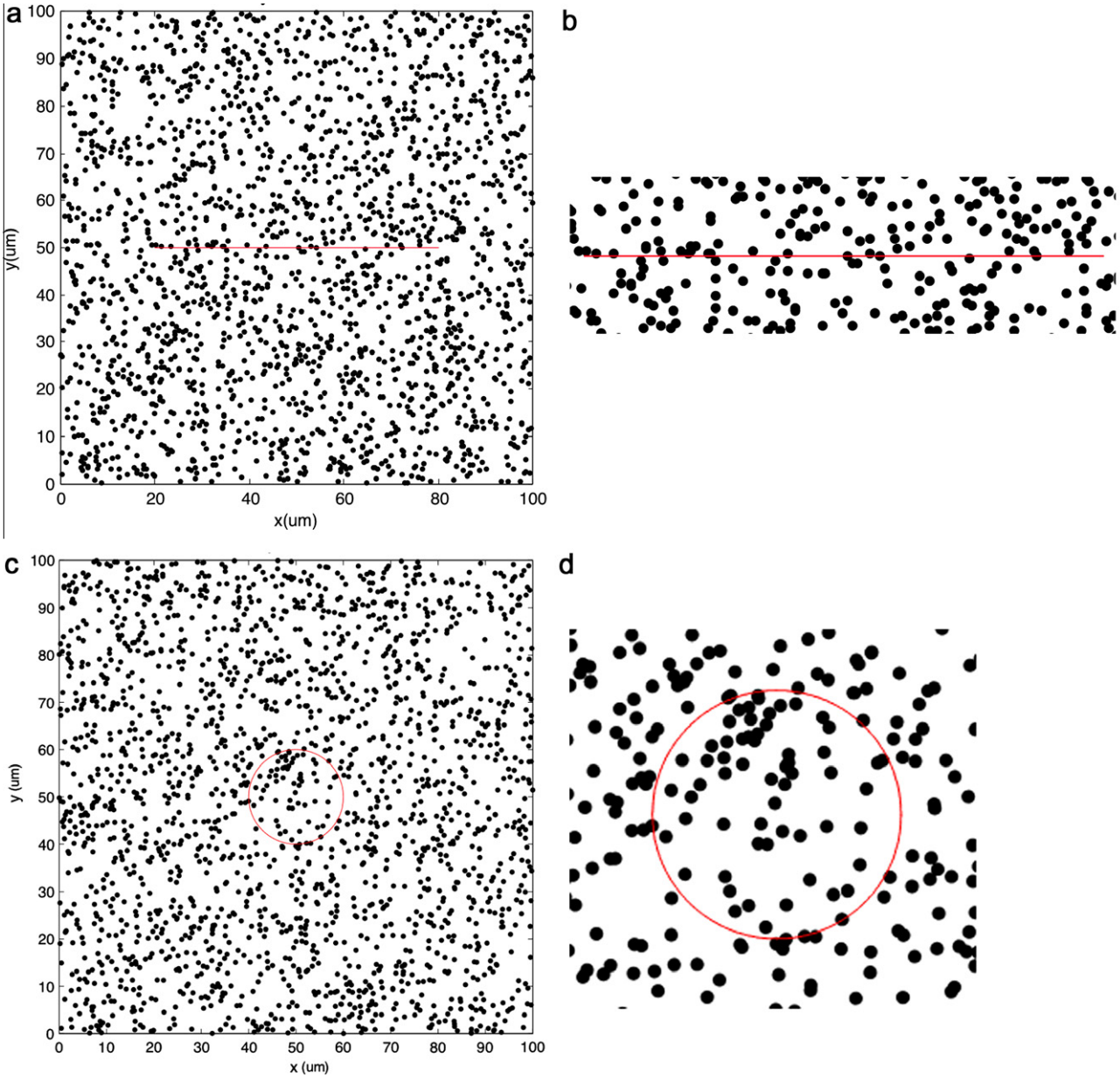

Fig. 10. (a) Monte Carlo simulation sample for the rectangular cross-section. (b) Magnification of (a) (the red line = 60 m). (c) Monte Carlo simulation sample for the circular cross-section. (d) Magnification of (c) (the red circle has a diameter of 20 m).

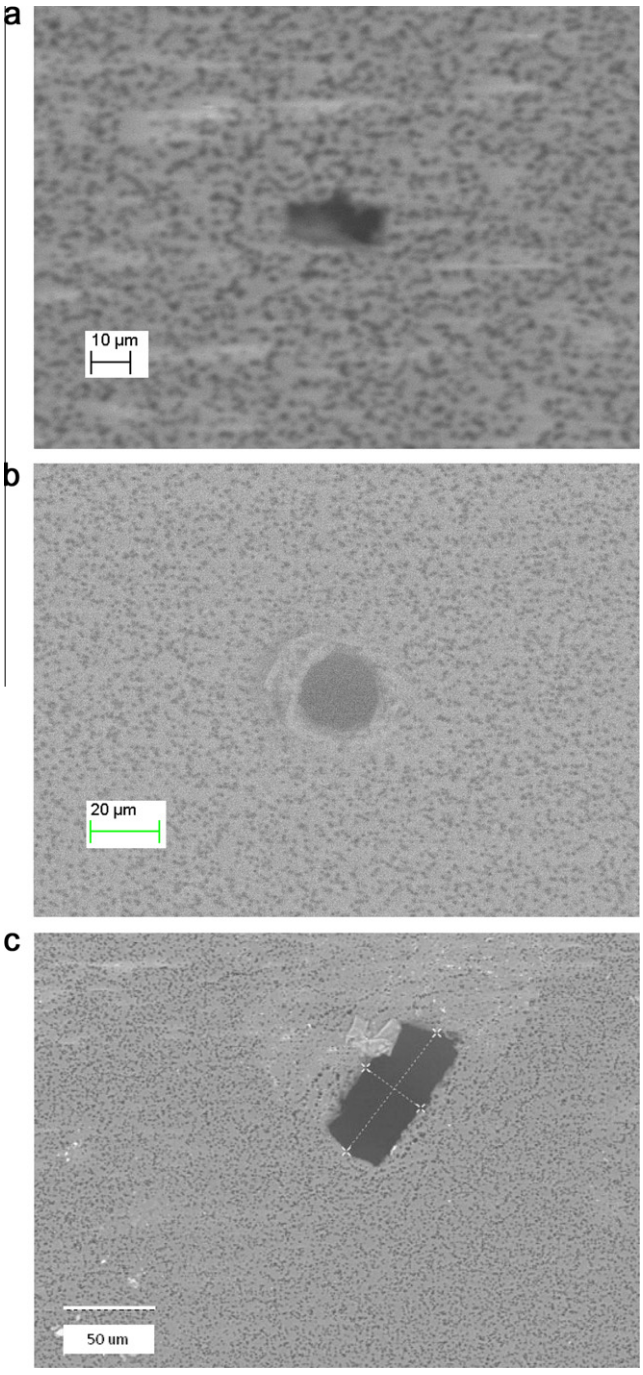

Fig. 11. (a) Footprint of the small rectangular probe on SPHMF. (b) Footprint of the small circular probe on SPHMF. (c) Footprint of the large rectangular probe on SPHMF.

4.3. Adhesive and cohesive strengths of NSES

The forces required for failure in the formulation inlays of the NSES samples were measured with a small rectangular probe with cross-section 10 × 20 μm, a small circular probe with a diameter of 20 μm, and one large probe with a cross-section of 45 × 90 μm. A total of 10 inlays were tested with each of these probes, yielding critical forces of 23.3 ± 6.6, 23.8 ± 2.9 and 81.2 ± 20.2 mN, respectively (mean ± SSD, Table 3). Since no curvature was observed (using the in situ video monitoring unit) for any test conducted with the small probe, there was no need to apply the Mohr–Coulomb theory in the computation of the cohesive shear strength of the formulation.

Table 3
Shear strength determined for NSES.

Probe size	Measured NSES formulation Critical force (mN)	Calculated NSES formulation Shear strength (MPa)
10 × 20 μm	23.3 ± 6.6	19.5 ± 5.5
45 × 90 μm	81.2 ± 20.2	2.03 ± 0.5
20 μm diameter	23.8 ± 2.9	18.9 ± 2.3

The failure modes in the tested structures were examined using SEM and EDS. These revealed that the large rectangular probe resulted in adhesive failure, as shown in Fig. 12a and b. In contrast, cohesive failure was always induced by the small probes. SEM revealed that a block of formulation inlay roughly the size of the small tip cross-section was dislodged, rather than the whole formulation inlay, as in the adhesive case (Fig. 12c and d). Note that there was a shallow circular footprint of the conical shoulder of the small probe immediately on top of the rectangular hole when the probe went deeper and pressed on the formulation. As the critical force was measured at the point of film failure the additional indentation did not have an impact on the results. Note also that for some of the cohesive failures deviation of the probes from the ideal positions in the FEM simulation may vary the stress distributions, but in these cases the stress distributions beneath the probe tip dominated and did not have an impact on the failure modes.

To obtain the shear strengths we assumed that the film covered the entire side wall length and reservoir width and that the film thickness in the center of the reservoir was 20 μm. Thus, by substituting the thickness of formulation in the central region of the reservoir h = 20 μm into Eq. (6) we can obtain the cohesive strength τ_c estimates: 19.5 ± 5.5 MPa for the small rectangular tip; 18.9 ± 2.3 MPa for the small circular probe (Table 3). The calculated cohesive strengths are statistically independent of the probe tip geometries and comparable with the shear strengths of plastics, e.g. 20.0 MPa for RIM polyurethane [10] and 23.5 MPa for HDPE [10].

Using Eq. (5) and taking the depth of the interface to be H = 100 μm, the adhesive strength of the NSES formulation inlay τ_i was calculated to be 2.03 ± 0.51 MPa (Table 3). This lower adhesive strength is attributed to the fact that adhesive failure corresponds to a condition in which a debond has extended across the interface. Hence, this represents a lower bound measurement of the strength required to overcome adhesive interactions, sliding friction and residual stress effects [15]. Further work is clearly needed to determine the relative contributions of such phenomena.

The above experimental results confirm the theoretical/computational predictions of a transition from cohesive failure (for small probe tips) to adhesive failure (for larger probe tips). While we recognize that the current model framework can successfully explain the phenomena observed in the current study, it is clear that further work is needed to develop fracture mechanics approaches that can model the effects of probe geometry and interfacial cracks on the robustness of suspended polymeric films, such as the ones studied here for model drug-eluting stents.

5. Concluding remarks

This paper presents the results of a combined experimental and computational study of the development of a novel technique to characterize the adhesion and cohesion strength of suspended polymeric films. The technique is not limited by the length scale

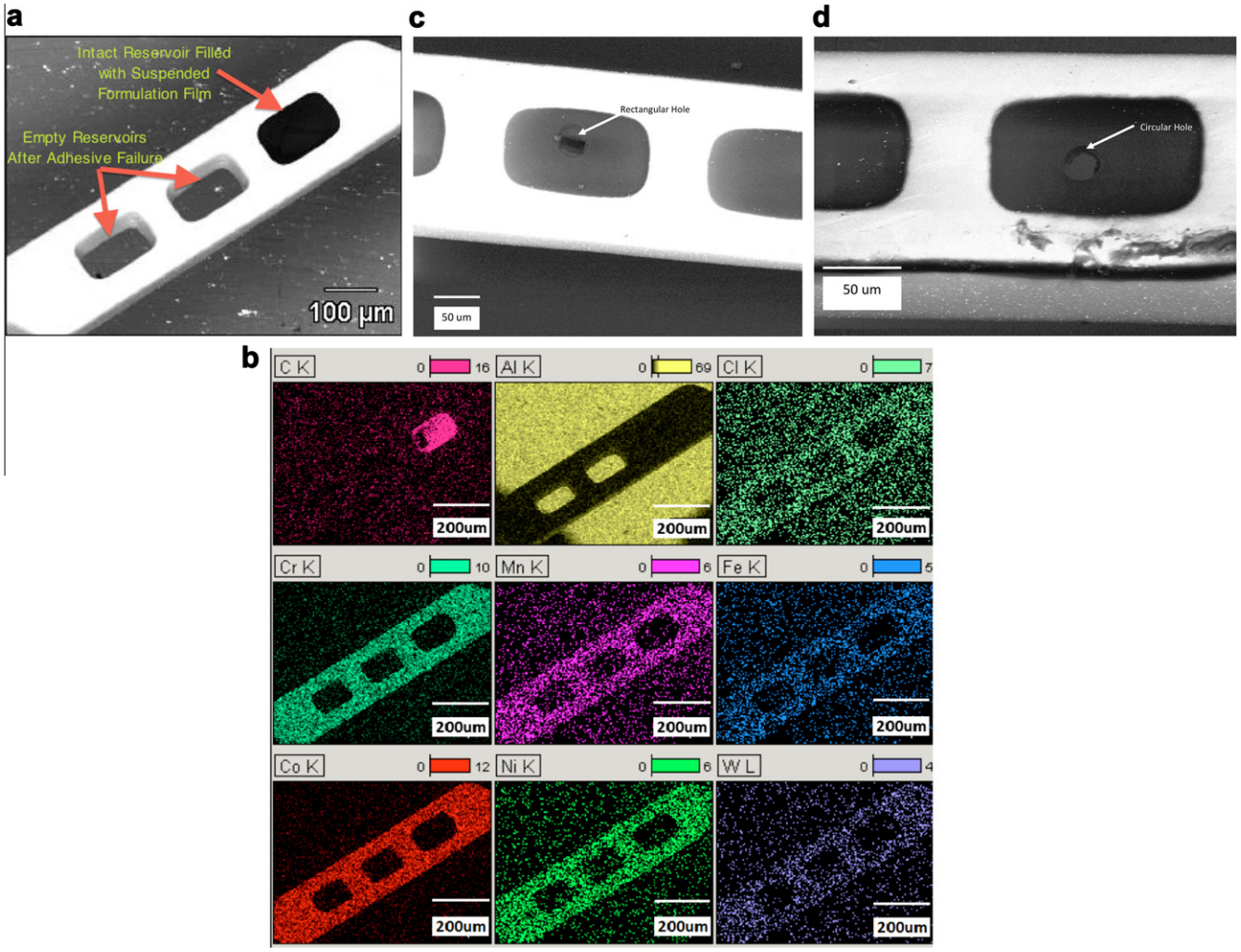

Fig. 12. (a) SEM micrographs for adhesive failure by the large probe. (b) EDS mapping results for adhesive failure by the large probe in (a). (c) SEM micrographs of cohesive failure by the small rectangular probe. (d) SEM micrographs of cohesive failure by the small circular probe.

of microstructures containing suspended polymeric films, as previously developed AFM and nanoindentation techniques. The performance of the testing technique was evaluated by conducting the test on standard materials, whose results were consistent with prior reports in the literature. The test technique was then applied to NSES, where the forces to induce cohesive or adhesive failure were obtained for a suspended polymeric formulation. The calculated cohesive shear strength is of the same order as that of plastics such as HDPE and reaction injection molding polyurethane. However, the adhesive strength is lower. The size of the probe tip has been shown to be critical in the transition from cohesive failure to adhesive failure. Fracture mechanics models are needed to evaluate the interfacial fracture toughness and crack growth.

Acknowledgements

The authors are grateful to Dr. Nan Yao and Dr. Gerald R. Poirier at the Princeton Institute for Science and Technology of Materials (PRISM) for discussions on the fabrication of tungsten probe tips. We also acknowledge use of the PRISM Imaging and Analysis Center, which is supported in part by the NSF MRSEC program through the Princeton Center for Complex Materials (grant DMR-0819860) and the Grand Challenges Program at Princeton University. This work was partly funded by the Cordis Corporation, a Johnson & Johnson Company.

Appendix A. Figures with essential color discrimination

Certain figures in this article, particularly Figures 2–5, 7–12, are difficult to interpret in black and white. The full color images can be found in the on-line version, at doi:10.1016/j.actbio.2011.12.018).

References

[1] Fattori R, Piva T. Drug-eluting stents in vascular intervention. Lancet 2003;361:247–9.
[2] Vodnick D, Nay R. Interfacial adhesion of viscoelastic coatings on medical stents, Hysitron application note. Eden Prairie, MN: Hysitron; 2011
[3] CSM Instruments. Application Note No. 8. Peseux, Switzerland: CSM Instruments; 1998.
[4] CSM Instruments. Application Note No. 17. Peseux, Switzerland: CSM Instruments; 2001.
[5] Burke M, Clarke B, Rochev Y, Gorelov A, Carroll W. Estimation of the strength of adhesion between a thermoresponsive polymer coatinig and nitinol wire. J Mater Sci Mater Med 2008;19:1971–9.
[6] Tang F, Ding N, Pacetti S. Nano-scratch adhesion evaluation of the XIENCE V™ drug eluting stent coating. In: Society for Biomaterials Annual Meeting; 2008.
[7] Wolf KV, Zong Z, Meng J, Orana A, Rahbar N, Balss KM, et al. An investigation of adhesion in drug-eluting stent layers. J Biomed Mater Res 2008;87A:272–81.
[8] Rahbar N, Wolf KV, Orana A, Fennimore R, Zong Z, Meng J, et al. Adhesion and interfacial fracture toughness between hard and soft materials. J Appl Phys 2008;104:103533–5.
[9] Meng J, Orana A, Tan T, Wolf KV, Rahbar N, Li H, et al. Adhesion and interfacial fracture in drug-eluting stents. J Mater Res 2010;25(4):641–7.

[10] ASTM. Standard D732-10: Standard Test Method for shear strength of plastics by punch tool. West Conshohocken, PA: ASTM International; 2010
[11] Coulomb CA. Essai sur une application des regles des maximis et minimis a quelquels problemesde statique relatifs, a la architecture. Mem Acad R Div Sav 1776;7:343–87.
[12] Conner RD, Dandliker RB, Johnson WL. Mechanical properties of tungsten and steel fiber reinforced $Zr^{41.25}Ti^{13.75}Cu^{12.5}Ni^{10}Be^{22.5}$ metallic glass matrix composites. Acta Mater 1998;46(17):6089–102.
[13] Marrey RV, Burgermeister R, Grishaber RB, Ritchie RO. Fatigue and life prediction for cobalt–chromium stents: a fracture mechanics analysis. Biomaterials 2006;27(9):1988–2000.
[14] Choi SH, Park TG. Synthesis and characterization of elastic PLGA/PCL/PLGA triblock copolymers. J Biomater Sci Polym Ed 2002;13(10):1163–73.
[15] Hsueh CH. Interracial debonding and fiber pull-out stresses of fiber-reinforced composites IV – sliding due to residual stresses. Mater Sci Eng A 1991;145:143–50.